Intensive disc-reverberation mapping of Fairall 9: first year of *Swift* and LCO monitoring

J. V. Hernández Santisteban [1]⋆ R. Edelson,[2]⋆ K. Horne,[1]⋆ J. M. Gelbord,[3,4] A. J. Barth [5]
E. M. Cackett,[6] M. R. Goad,[7] H. Netzer,[8] D. Starkey,[1] P. Uttley,[9] W. N. Brandt,[10,11,12]
K. Korista,[13] A. M. Lohfink,[14] C. A. Onken [15,16] K. L. Page [7] M. Siegel,[10] M. Vestergaard,[17]
S. Bisogni [18] A. A. Breeveld,[19] S. B. Cenko,[20,21] E. Dalla Bontà [22,23] P. A. Evans [7] G. Ferland,[24]
D. H. Gonzalez-Buitrago,[25] D. Grupe [26] M. D. Joner,[27] G. Kriss [28] S. J. LaPorte,[29] S. Mathur,[30,31]
F. Marshall,[32] M. Mehdipour,[33] D. Mudd [5] B. M. Peterson,[28,30,31] T. Schmidt,[5] S. Vaughan[7] and
S. Valenti[34]

Affiliations are listed at the end of the paper

ABSTRACT

We present results of time-series analysis of the first year of the Fairall 9 intensive disc-reverberation campaign. We used *Swift* and the Las Cumbres Observatory global telescope network to continuously monitor Fairall 9 from X-rays to near-infrared at a daily to subdaily cadence. The cross-correlation function between bands provides evidence for a lag spectrum consistent with the $\tau \propto \lambda^{4/3}$ scaling expected for an optically thick, geometrically thin blackbody accretion disc. Decomposing the flux into constant and variable components, the variable component's spectral energy distribution is slightly steeper than the standard accretion disc prediction. We find evidence at the Balmer edge in both the lag and flux spectra for an additional bound-free continuum contribution that may arise from reprocessing in the broad-line region. The inferred driving light curve suggests two distinct components, a rapidly variable (<4 d) component arising from X-ray reprocessing, and a more slowly varying (>100 d) component with an opposite lag to the reverberation signal.

Key words: accretion, accretion discs – galaxies: active – quasars: individual: Fairall 9.

1 INTRODUCTION

Accretion discs around supermassive black holes (BHs) power the most energetic persistent sources in the Universe (Salpeter 1964; Zel'dovich 1964; Lynden-Bell 1969). These active galactic nuclei (AGN) allow BHs to grow throughout cosmic time (Brandt & Alexander 2015) and play a major role in the formation history of galaxies (Fabian 2012). However, the combination of large distances and small angular scales precludes us from directly imaging the central engine and the vicinity of the BH. Despite the recent progress in observing the broad-line region (BLR) via near-infrared (IR) interferometric observations (Gravity Collaboration et al. 2018), the accretion disc itself is a few orders of magnitude smaller and mostly out of reach for current instrumentation (besides the notable example of M87∗; Event Horizon Telescope Collaboration et al. 2019).

It is possible to use the variable nature of AGN as a mean to access information on scales well below any spatial resolution limit required to directly detect the accretion disc by imaging. By measuring the time-delayed response between the continuum light (originating in the disc) and the BLR, it is viable to infer the mass of the BH. This method, commonly known as reverberation mapping (Blandford & McKee 1982; Peterson et al. 2004), has been an efficient technique to

measure a sizeable sample of BH masses spanning a broad range of luminosities and redshifts (e.g. Bentz & Katz 2015; Grier et al. 2017).

This same basic principle can be used to study the smaller 'central engines' of AGN. Fluctuations in the final stage of the accretion flow modulate the flux of high-energy photons (mostly X-rays and EUV) from a hot plasma in the vicinity of the BH. These have been proposed to provide the main driver for the variability observed at ultraviolet (UV), optical, and IR wavelengths. These high-energy fluctuations propagate outwards at the speed of light. They act as a flickering lamp-post above the BH that illuminates the surface of the accretion disc. As light travels further away from the central-most regions surrounding the BH, the high-energy fluctuations are 'echoed' in the disc as they are absorbed and re-emitted at lower energies set by the local disc temperature. In addition, the characteristic time delay between wavelengths/bands $[\tau(\lambda)]$ traces the average emitting radius between zones in the accretion disc, allowing probe of its size and radial temperature profile (Cackett, Horne & Winkler 2007).

Continuum reverberation mapping has progressed in the last few years as a result of ambitious programmes such as the Space Telescope and Optical Reverberation Mapping Project (STORM; e.g. De Rosa et al. 2015; Edelson et al. 2015; Fausnaugh et al. 2016; Starkey et al. 2017) and other intensive disc-reverberation mapping (IDRM) campaigns (Edelson et al. 2017, 2019; Cackett et al. 2018; McHardy et al. 2018), which have found discrepancies with the standard accretion theory (Shakura & Sunyaev 1973). In

⋆ E-mail: pantro@gmail.com (JVHS); rickedelson@gmail.com (RE); kdh1@st-andrews.ac.uk (KH)

particular, IDRM campaigns with the Neil Gehrels *Swift* Observatory (*Swift* hereafter; Gehrels et al. 2004) X-ray and UV/optical telescopes (UVOT) have provided continuum-lag measurements for a sample of AGN, finding implied accretion disc sizes up to a factor of ∼3 times larger than predicted (e.g. Pooley et al. 2007; Edelson et al. 2019). In addition, deviations from the canonical expectations of lag as a function of wavelength ($\tau \propto \lambda^{4/3}$) in particular bands (e.g. *U* band: Edelson et al. 2015; Fausnaugh et al. 2016; Cackett et al. 2018) may point to a significant contribution of the 'diffuse continuum emission' (DCE) from the BLR (Korista & Goad 2001; Lawther et al. 2018; Chelouche, Pozo Nuñez & Kaspi 2019; Korista & Goad 2019; Netzer 2020) or a different temperature profile across the disc (Starkey et al. 2017). Furthermore, the apparent disconnect between the X-rays and UV/optical wavelengths (i.e. driver and reprocessed light, respectively) may require additional reprocessing components beyond the simple accretion disc model (e.g. Gardner & Done 2017).

The focus of this paper is the Seyfert 1 galaxy Fairall 9 (Fairall 1977; Ricker 1978). It is a relatively nearby AGN ($z = 0.047$; Hawley & Phillips 1978) with a central BH $M = 2.55 \pm 0.56 \times 10^8$ M$_\odot$ (Peterson et al. 2004). Several X-ray studies have determined a low extinction and a lack of warm absorber (Emmanoulopoulos et al. 2011) in Fairall 9. In addition, the persistent spectral components (Lohfink et al. 2016) suggest a clear view of the inner flow around its central engine. Initial variability studies found correlated X-ray and UV emission on scales <4 d (Lohfink et al. 2014). Fairall 9 has also been a target of continuum reverberation mapping using *Swift* (Pal et al. 2017) where inter-band lags were found to be consistent with $\tau \propto \lambda^{4/3}$, albeit with large uncertainties. This failure to detect a clear inter-band lag is mostly due to the low-cadence sampling (∼2–7 d) and a lack of information at longer (ground-based) wavelengths in that earlier experiment.

In this paper, we present the analysis and results of the first year (2018 May–2019 February) of the IDRM campaign Key Projects[1] with *Swift* and Las Cumbres Observatory global telescope network (LCO hereafter; Brown et al. 2013) on Fairall 9. In Section 2, we describe the multimission campaign as well as the data reduction and calibration. We employ the light curves to perform time-series analysis in Section 3 and present the wavelength-dependent lags in Section 4. Finally, we summarize our results in Section 5.

2 OBSERVATIONS

Fairall 9 is currently the subject of a 1.7-year IDRM campaign built around observations with *Swift* and LCO. This paper reports the results of roughly the first half of this campaign, covering MJD 58250–58550. *Swift* monitored the target on an approximately daily basis in the 0.3–10 keV X-rays and six broad-band UV/optical filters (*UVW2, UVM2, UVW1, U, B, V*) spanning ∼1900–5500 Å, and LCO performed $uBVg'r'i'z_s$ photometry approximately three times per day (once per day at each southern site, in Chile, Australia, and South Africa). This much denser ground-based sampling aimed to compensate for a higher data loss rate, due to weather and equipment issues. The first year of data from these two instruments form the basis of this work. Additional monitoring was obtained, e.g. LCO optical spectroscopy and *NICER* X-ray spectroscopy; those results will be reported elsewhere.

2.1 *Swift*-XRT

Data from two of *Swift*'s three instruments are used in this paper: the X-Ray Telescope (XRT; Burrows et al. 2005) and the UVOT (Roming et al. 2005). All XRT observations were made in photon counting (PC) mode. The XRT data are analysed using the standard *Swift* analysis tools described by Evans et al. (2009).[2] These produce light curves that are fully corrected for instrumental effects such as pile up, dead regions on the CCD, and vignetting. The source aperture varies dynamically according to the source brightness and position on the detector.

We output the observation times (the midpoint between the start and end times) in MJD for ease of comparison with the UVOT data. We utilize 'snapshot' binning, which produces one bin for each continuous spacecraft pointing. This is done because these short visits always occur completely within one orbit with one set of corresponding exposures in the UVOT filters. In all other cases, we used the default values. We generated an X-ray light curve covering the full XRT bandpass (XF; 0.3–10 keV). For a detailed discussion of this tool and the default parameter values, please see Evans et al. (2009).

2.2 *Swift* UVOT

This paper's UVOT data reduction follows the same general procedure described in our previous work (e.g. Edelson et al. 2019). This process has three steps: flux measurement, removal of points that fail quality checks, and identification and masking of low-sensitivity regions of the detector. Each step is described in turn below.

All data were reprocessed for uniformity (using version 6.22.1 of `heasoft`) and their astrometry refined (following the procedure of Edelson et al. 2015) before measuring fluxes using `uvotsource` from the `ftools`[3] package (Blackburn 1995). The filters and other details of this instrument are given in Poole et al. (2008) and Breeveld et al. (2011). Source photometry was measured in a circular extraction region of 5 arcsec in radius, while backgrounds were taken from concentric 40–90 arcsec annuli. In the *V* band in particular, especially when the AGN power is lower, the galaxy contributes significantly to the measured flux. The final flux values include corrections for aperture losses, coincidence losses, large-scale variations in the detector sensitivity across the image plane, and declining sensitivity of the instrument over time.

In the second step, the resulting measurements are used for both automated quality checks and to flag individual observations for manual inspection. These automated checks include aperture ratio screenings to catch instances of extended point spread functions (PSFs) or when the astrometric solution is off, and a minimum exposure time threshold of 20 s. Data are flagged for inspection when the fitted PSFs of either the AGN or several field stars were found to be unusually large or asymmetric, or if fewer than 10 field stars with robust centroid positions are available for astrometric refinement. Upon inspection, observations are rejected if there are obvious astrometric errors, doubled or distorted PSFs, or prominent image artefacts (e.g. readout streaks or scattered light) that would affect the AGN measurement. Note that we adopt a non-standard setting of 7.5 per cent for the `uvotsource` parameter `fwhmsig` because this yields flux uncertainties more consistent with Gaussian statistics (Edelson et al. 2017).

The third step screens out data that fall within detector regions with reduced sensitivity. In our previous work, these regions were

---

identified through a bootstrap method based on the prominent low outliers from the AGN light curves (e.g. Edelson et al. 2019). We have now mapped the sensitivity variations with more uniform, higher resolution coverage across the entire detector creating sensitivity masks for each filter, based on an independent set of data. This process is described in Appendix A. The light curves that result after applying these masks are shown in Fig. 1.

2.3 Las Cumbres Observatory

We obtained a multicolour light curve by using the LCO network's 1-m robotic telescopes to monitor Fairall 9, as part of the 2018B AGN Key project. Our observations were obtained with an average cadence of three observations per day, one at each of the southern LCO sites located at Sutherland (South Africa), Cerro Tololo (Chile), and Siding Spring (Australia). Each observation consisted of two consecutive exposures with the Sinistro CCD camera, to mitigate the impact of cosmic ray hits and to provide an internal consistency check on the uncertainties. In total, 6109 individual exposures were taken in seven bands: B, V, u', g', r', i', and z_s. A summary of the observations is presented in Table 1.

The data extracted from the LCO archive were bias and flat-field corrected images pipeline processed with BANZAI (McCully et al. 2018). We extracted multiaperture aperture photometry with SEXTRACTOR (Bertin & Arnouts 1996) on every image. We constructed a global background model by smoothing the image in a 200-pixel mesh, large enough to avoid the extended sources influencing the background estimate. After subtracting the background model and performing the aperture photometry, we constructed a curve of growth for each individual frame and measured the correction factor required to bring every star flux as if extracted from an azimuthally averaged PSF. This method produced stable light curves which were more robust to the diverse range of atmospheric conditions (e.g. airmass, seeing) taken throughout the year, without performing PSF extraction. The colour-correction and atmospheric extinction coefficients were obtained from Valenti et al. (2016) and applied before the photometric calibration. We used comparison stars in each field to perform an image zero-point calibration at each epoch. We used the AAVSO Photometric All-Sky Survey (APASS) DR10 (Henden et al. 2018) for all LCO filters except the *u* band, for which no APASS information was available. Here, we made use of the *Swift*/UVOT *U*-band images to obtain the fluxes of reference stars in the field. We applied a 3σ clipping to the zero-point estimates and perform a bootstrap method to obtain the error on the zero-point. The full light curves for year 1 are shown in Fig. 1 and the data format is shown in Table B1.

After these corrections, we noted small but significant systematic offsets among the light curves from different sites and telescopes in the LCO network, in particular for the *B* band (see Fig. 2), but evident also at *g'* and z_s. We therefore performed an inter-telescope calibration, as described below, which reduced the offsets to obtain the light curves shown in Fig. 1.

2.3.1 Intercalibration of the LCO light curves

A total of eight LCO 1-m telescopes on three southern continents were used in this campaign. Despite the fact that identical designs were used for the telescopes, detectors, and filter sets, we detected small systematic offsets, as shown in Fig. 2. Thus, we found it necessary to recalibrate the light curves we extracted from the CCD images taken by these different telescopes. This was done

in a three-step process. First, the data are separated by band with unique identifiers noted for each of these eight telescopes. Then for each data point, the ratio of the reported flux to that of all other fluxes gathered (a) within 2 d and (b) on different telescopes is determined. Then for each unique band/telescope combination, the mean of this ratio is determined and all fluxes and errors divided by this mean amount. This yields better-intercalibrated fluxes with smaller dispersion around the mean value in all bands.

Thus, the second step is to iterate this process, a total of six times, until the changes in this calibration factor become negligible. The final result is effectively a first-order (multiplicative) intercalibration of the telescopes.

This strategy corrects the measured fluxes but does not affect the reported uncertainties, which are still small compared to the short-term dispersion within these data. That is, systematic calibration errors are still present and must be quantified. Thus, the third step adjusted the reported uncertainties by determining an additional 'inter-telescope calibration error' term to be added in quadrature to the reported uncertainties. This is done by first taking the previously calibrated flux values in each band (no longer segregating by telescope) and measuring the absolute values of the point-to-point differences between successive points, i.e. the moving range $MR_i = |x_i - x_{i-1}|$. We then use the factors method to estimate of the total short-term dispersion $\sigma_{dis} = d_2 \cdot \langle MR_i \rangle$, where the $d_2 = 1.128$ is the unbias factor[4] (Wheeler & Chambers 1992). We assume that intrinsic variations are small compared to the errors on the data on these time-scales as the average sampling is $\sim$0.7 d in this well-sampled data set. Then we determine the additional variance that, when added to the sum of the squares of the observed errors, yields the total variance implied by the short-term dispersion. Values for each telescope and filter are shown in Appendix B and Table B2. The amplitude of this additional error term (the square root of the additional variance) ranges from 0.58 per cent of the mean flux in the best band (*r*) to 1.23 per cent in the worst bands (*B* and *z*). In all cases, it is much larger, typically by a factor of 3–6, than the uncorrected errors. Thus, we conclude that inter-telescope calibration is the dominant source of error in our LCO light curves.

3 TIME-SERIES ANALYSIS

3.1 Cross-correlation function

Cross-correlation functions (CCFs) were measured using the interpolated CCF (Gaskell & Peterson 1987). We used the sour code,[5] which is based on the specific implementation presented in Peterson et al. (2004). We first normalized the data by subtracting the mean and dividing by the standard deviation. These were derived 'locally' – only the portions of the light curves that are overlapping in time for a given lag are used to compute these quantities. As discussed by White & Peterson (1994), 'global' normalization using the entire light curve is appropriate for stationary variability processes but local normalization is more appropriate for weakly non-stationary variability, as has been observed to be the case in AGN. Due to the uneven sampling of the light curves, we require to perform an interpolation to properly perform any CCF analysis. We implemented '2-way' interpolation, which means that for each pair of bands, we first interpolated in the 'reference' band and then measured

---

[4] $d_2 = 1.128$ is the expected value of the range of two observations from a normal population with standard deviation = 1.
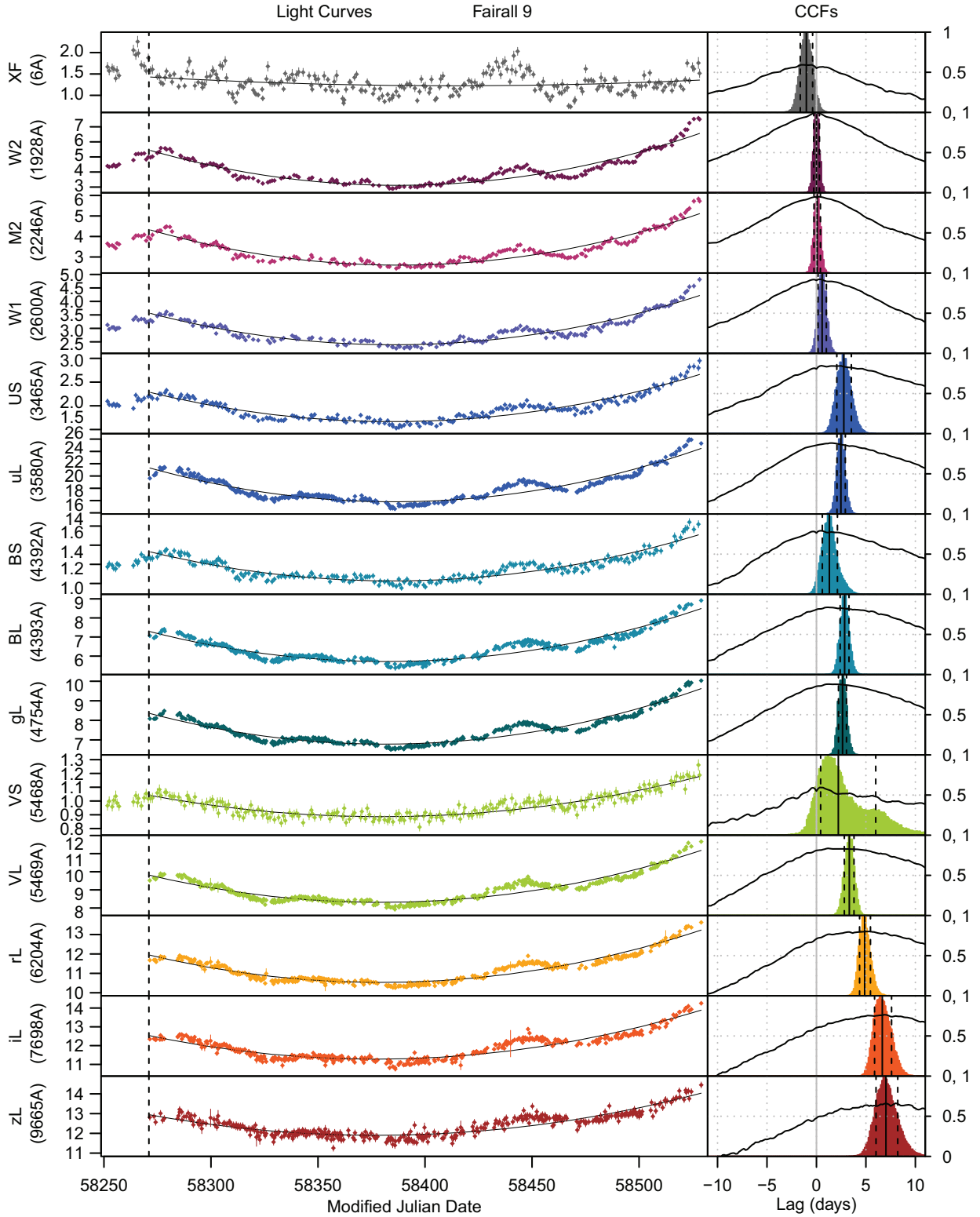[5] This code is available at https://github.com/svdataman/sour.

Figure 1. Left-hand panel: *Swift* and LCO light curves for Fairall 9. Data are ordered by wavelength, with the top panel the X-ray data from the XRT, the next 3 the UV light curves from the UVOT, and the remaining 10 the optical light curves from both the UVOT and LCO. *Swift* optical UVOT data are denoted by an 'S' and the LCO optical data by an 'L'. The X-ray data are in units of count s^{-1} and the optical data are all in units of mJy. A second-order fit to the data, which was subtracted before performing the CCF analysis so as to remove excess low-frequency power, is shown as a black line. Only data gathered after MJD 58271 were used in the CCF analysis so that the *Swift* and LCO data used cover the same time period. Right-hand panel: CCFs (in black; scale on the right-hand side) and FR/RSS centroid distributions (in colour) for each band relative to the *W2* band. A positive value means the comparison band lags behind *W2*. The median of the distribution and its 1σ confidence intervals are shown as black solid and dashed lines, respectively. These values are presented in Table 1.

Table 1. Observation log and light-curve properties of the first year of Fairall 9 campaign with *Swift* and LCO. The errorbars represent the 1σ confidence interval.

Filter	λ_{eff}	t_{exp}	Epochs	Δt_{mean}	Δt_{med}	$\langle F_\nu \rangle$	F_ν host	F_{var}	r_{max}	τ_{CCF}	1σ (16 per cent, 84 per cent)	τ_{cream}
	(Å)	(s)		(d)	(d)	(mJy)	(mJy)			(d)		(d)
	(1)	(2)	(3)	(4)	(5)	(6)	(7)	(8)	(9)	(10)	(11)	(12)
Swift										CCF	CCF	CREAM
XF	6	1000	263	1.074	0.997	...	. ...	$0.184 \pm 0.004.$	0.594	-1.02	$(-1.63, -0.39)$	
W2	1928	333	240	1.184	0.998	5.93 ± 0.08	0.12 ± 0.12	0.227 ± 0.001	1.0	0.0	$(-0.27, 0.31)$	0.00 ± 0.10
M2	2246	250	235	1.209	1.006	5.98 ± 0.24	0.61 ± 0.13	0.204 ± 0.001	0.95	0.08	$(-0.25, 0.40)$	0.25 ± 0.11
W1	2600	167	232	1.225	1.048	5.86 ± 0.23	1.65 ± 0.12	0.166 ± 0.001	0.922	0.58	$(0.17, 1.00)$	0.55 ± 0.13
U	3465	83	247	1.150	0.999	5.72 ± 0.22	3.04 ± 0.12	0.134 ± 0.002	0.846	2.77	$(2.06, 3.53)$	1.33 ± 0.17
B	4392	83	255	1.114	0.998	4.34 ± 0.20	3.90 ± 0.09	0.107 ± 0.002	0.791	1.3	$(0.60, 2.12)$	2.26 ± 0.23
V	5468	83	247	1.150	1.001	3.99 ± 0.23	6.26 ± 0.08	0.076 ± 0.002	0.595	2.22	$(0.43, 6.00)$	3.35 ± 0.28
LCO												
u'	3580	300	874	0.357	0.121	5.42 ± 0.18	2.87 ± 0.11	0.117 ± 0.002	0.883	2.47	$(2.07, 2.92)$	1.33 ± 0.17
B	4392	60	914	0.322	0.039	4.35 ± 0.13	2.92 ± 0.09	0.105 ± 0.002	0.837	2.85	$(2.40, 3.29)$	2.26 ± 0.23
g'	4770	60	861	0.355	0.059	4.43 ± 0.13	3.94 ± 0.09	0.092 ± 0.001	0.881	2.64	$(2.23, 3.04)$	2.64 ± 0.25
V	5468	60	850	0.411	0.077	4.48 ± 0.14	5.42 ± 0.09	0.077 ± 0.001	0.836	3.32	$(2.82, 3.80)$	3.35 ± 0.28
r'	6215	60	857	0.432	0.072	4.17 ± 0.13	7.84 ± 0.09	0.058 ± 0.001	0.802	4.88	$(4.36, 5.46)$	4.08 ± 0.30
i'	7545	60	880	0.419	0.064	4.01 ± 0.14	8.68 ± 0.08	0.055 ± 0.001	0.764	6.66	$(5.88, 7.59)$	5.26 ± 0.30
z_s	8700	120	828	0.360	0.055	3.32 ± 0.13	9.75 ± 0.07	0.044 ± 0.001	0.662	7.03	$(6.02, 8.22)$	6.12 ± 0.29

Notes. (1) λ_{eff} is the effective wavelength at each band; (2) t_{exp} is the individual exposure time of each frame. The *Swift* exposure times are the average for a 1-ks exposure for *Swift* UVOT mode 0x30ed; (3) epochs are the number of independent measurements; (4) mean and (5) median time between consecutive images in each filter; (6) $\langle F_\nu \rangle$ is the average flux density of the variable component and (7) $\langle F_\nu \rangle$ host, for the underlying host galaxy; (8) F_{var} is the fractional variability as described in Fausnaugh et al. (2016); (9) r_{max} is the maximum correlation coefficient from the CCF analysis; (10) τ_{CCF} is the median value in the inter-band lag distribution its 1σ 16 and 84 per cent confidence interval (11); (12) τ_{cream} are the mean values of the delay distributions as measured with CREAM. All lag measurements for CCF and CREAM are shown in reference to the *W2* band.
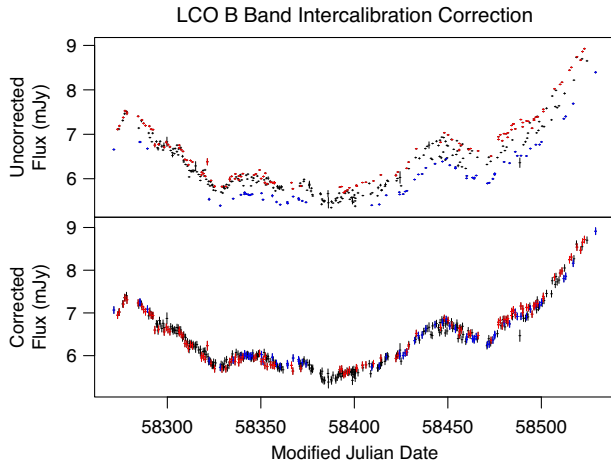

Figure 2. LCO *B*-band light curve of Fairall 9 showing the data before and after the inter-telescope flux recalibration. Eight of the LCO southern telescopes were used to monitor Fairall 9, at sites in Chile, South Africa, and Australia. Data from the Chilean '1m004' and '1m005' LCO telescopes are shown in blue and red, respectively, while those for the other six telescopes (in all three sites) are shown in black. Note that in the upper panel, the (uncorrected) red and blue light curves differ by many times the errors, while in the lower panel, the (corrected) data appear consistent within the final errors. The recalibration process is discussed in Section 2.3.1.

the correlation function, next interpolated in the 'subsidiary' band and measured the correlation, and subsequently averaged the two to produce the final CCF. This was done because the alternative '1-way' interpolation produces an autocorrelation function that is not strictly symmetric, which, as an even function, it should be. The *W2* light

curve is always the reference and the other bands are considered the subsidiary bands in this analysis. This band was chosen because it has the shortest UV wavelength and thus is closest to the thermal peak of the accretion disc. The CCF ($r(\tau)$, where τ is the lag) is then measured and presented to the right-hand side of the light curves in Fig. 1.

We then used the 'flux randomization/random subset selection' (FR/RSS) method (Peterson et al. 1998) to estimate uncertainties on the measured lags. This is a Monte Carlo technique in which lags are measured from multiple realizations of the CCF. The FR aspect of this technique perturbs in a given realization each flux point consistent with the quoted uncertainties assuming a Gaussian distribution of errors. In addition, for a time series with N data points, the RSS randomly draws with replacement N points from the time series to create a new time series. In that new time series, the data points selected more than once have their error bars decreased by a factor of $n_{rep}^{-1/2}$, where n_{rep} is the number of repeated points. Typically, a fraction of $(1 - (1/n))^n \rightarrow 1/e$ of data points is not selected for each RSS realization. In this paper, the FR/RSS is applied to both the 'reference' and subsidiary light curves in each CCF pair. The CCF ($[r(\tau)]$, where τ is the lag) is then measured and a lag determined to be the weighted mean of all points with $r > 0.8 r_{max}$, where r_{max} is the maximum value obtained for the correlation coefficient r (e.g. Edelson et al. 2019). Values for every band are given in Table 1. For the data presented herein, lags are determined for 55 000 realizations and then used to derive the median centroid lag and 68 per cent confidence intervals, also presented in Table 1. This number of trials was chosen so that uncertainties on the derived median lags and confidence intervals due to sample statistics are negligible. Repeating this test confirms that these quantities change by only very small amounts compared to the widths of the confidence intervals.

3.2 CREAM light-curve modelling

Following Starkey, Horne & Villforth (2016) and Starkey et al. (2017), we fit the *Swift* and LCO light curves using the CREAM[6] reverberating accretion disc model in order to retrieve physical parameters from the system. Here, we briefly discuss the reverberation methodology. CREAM models the delay distribution of the accretion disc at every wavelength, assuming local reprocessing of the high-energy photons and re-emission as a blackbody spectrum. For the standard accretion disc temperature profile, $T^4 \propto M \dot{M} R^{-3}$, the mean time delay scales as $\langle \tau \rangle \propto \left(M \dot{M} \right)^{1/3} \lambda^{4/3}$. Thus, by using multiwavelength data, we can fit for the product $M \dot{M}$, given by the average delay of the individual light curves. Since the lamp-post model assumes that the same compact source is responsible for driving the variations in all of the echo light curves, it is necessary to define the driving light curve. CREAM builds an independent model for this driving light curve (as opposed to other methods that require one to be provided) using a damped-random walk (DRW) model as a prior. Each echo light curve is then modelled at their corresponding wavelengths by convolving the driving light curve with the best-fitting delay distribution, and then scaled by a multiplicative factor and shifted by an additive constant. We explore the parameter space using a Markov chain Monte Carlo (MCMC) procedure to find the posterior distributions of the parameters of interest.

We have used a face-on disc ($i = 0$, the effect of inclination angle on the measurement of the delay spectrum is very small, as shown in Starkey et al. 2016) and a standard temperature profile $T \propto R^{-3/4}$. The noise model contains an extra scatter term added in quadrature for each light curve. The driving light curve has a fixed maximum Fourier frequency of $\nu_{\max} = 2\pi/\Delta t_{\mathrm{mean}} = 1.0$ cycles d^{-1}, set by the average time separation between observations in the LCO bands (see Table 1). We ran the MCMC procedure for 10^5 iterations where we judged that the chains had adequately sampled the posterior distributions of the model parameters. We discarded the first 20 000 chains as burn-in.

We made an initial fit (Model 1) using the full light curves with no detrending. This resulted in delay distributions with mean lags that were shorter by a factor of $\sim$2–3 than those obtained via CCF. Since CREAM generates the driving light curve instead of using one as a reference (as in the case of CCF), we can compare it directly to the X-ray light curve to test whether the latter is the main driver of the reprocessing. In the first panel of Fig. 3, we show the driving light curve, which presents a long-term variation that is not present in the X-ray one (shown in the second panel), and most likely not arising from the reprocessing itself. However, variability superimposed on this slow and smooth trend is visible, at shorter time-scales (of the order of days) compatible with a reverberation signal. To test this, we fitted a quadratic polynomial to the driving light curve to focus on the shorter time-scale, shown in the second panel of Fig. 3. The residual variability now resembles qualitatively the 0.3–10 keV X-ray light curve, albeit with a discernible lag between them. This particularly notable in the bump around MJD 58440.

In order for the delay distribution to be modified by this slow component, it must carry an intrinsic time dependence in addition to the dilution of the amplitude of the signal. We discuss this component in further detail in Section 4.4. Motivated by this result, we performed a second fit with CREAM (Model 2) with the same parameters and priors described earlier after subtracting the quadratic detrending,
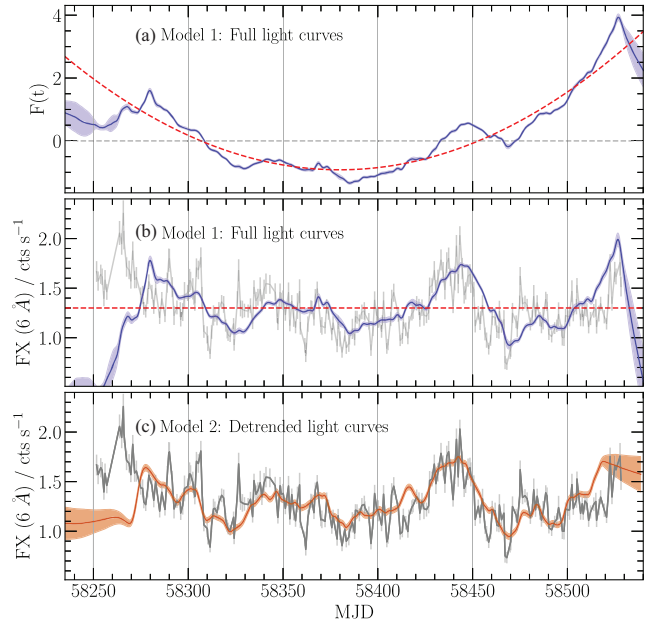
---

[6]The PYTHON implementation of this software PYCECREAM can be found at https://github.com/dstarkey23/pycecream.

Figure 3. Panel (a): driving light curve derived by CREAM with its 68 per cent confidence interval as the contours for the fit to the full light curves. A quadratic fit used to detrend is shown as the red dashed line. Panel (b): comparison between the full *Swift* X-ray 0.3–10 keV light curve and the driving light curve after subtracting a quadratic trend. The driving light curve has been scaled to match the X-ray one. A clear shift between these two light curves is observed. Panel (c): driving light curve obtained from the fitting of the detrended light curves with CREAM compared to X-rays.

i.e. using the same signal as those used by the CCF analysis. The resulting fit to each light curve, residuals of the fit, and the delay distributions for each band are shown in Appendix C, Figs C1 and C2. By removing this slow component, we recovered a lag spectrum with values that match closely to those obtained by CCF, shown in reference to the *UVW2* band in Table 1. We note that the largest disagreements between CCF and CREAM are in the *U* and *i* band, likely arising from the contribution of the diffuse continuum emission (see Section 4.3 for further discussion) that currently CREAM does not incorporate and only assumes the disc $\tau \propto \lambda^{4/3}$ lag distribution. Furthermore, the driving light curve inferred now directly resembles the X-ray light curve shown in the two bottom panels of Fig. 3. The mismatch between the driving light curve and the X-rays at both ends is caused by the inadequate representation of the smooth component as a parabola. Since this component flattens out during, the parabola overpredicts the contribution thus resulting in large residuals.

This indicates that there are (at least) two processes that contribute to the overall variability of Fairall 9 and that the observed X-rays cannot be the sole driving mechanism of variability at optical wavelengths (see further discussion in Section 4.4). In order to address the origin of such long-term variability, we require a larger time baseline. Thus, continuing the multiyear monitoring of Fairall 9 is paramount.

The CREAM fit estimates the posterior probability distribution of the product $M \dot{M}$. We find a very well-determined value of $\log(M \dot{M}/\mathrm{M}_\odot^2\,\mathrm{yr}^{-1}) = 7.49 \pm 0.07$. Assuming a $2.55 \times 10^8\,\mathrm{M}_\odot$ BH (Peterson et al. 2004), the Eddington ratio is therefore $\dot{m}_{Edd} = 0.020 \pm 0.004$, consistent with the value determined from X-ray studies (Vasudevan & Fabian 2009).

Table 2. Best-fitting parameters to the inter-band lag spectrum.

Parameter	No X-rays		Including X-rays		Including X-rays and no *U* band	
	α fixed	α free	α fixed	α free	α fixed	α free
τ_0/d	1.20 ± 0.10	2.32 ± 1.65	1.20 ± 0.09	1.40 ± 0.48	1.19 ± 0.08	1.32 ± 0.46
α	4/3	0.93 ± 0.39	4/3	1.22 ± 0.22	4/3	1.26 ± 0.23
y_0	0.92 ± 0.16	1.02 ± 0.09	0.91 ± 0.15	0.93 ± 0.13	0.94 ± 0.15	0.95 ± 0.15
χ_ν^2	1.16	1.17	1.09	1.175	1.017	1.118
d.o.f	11	10	12	11	10	9

4 RESULTS

4.1 Inter-band lag fits

The standard model for lamp-post irradiation of a thin accretion disc predicts a lag-wavelength dependence of $\tau \propto \lambda^{4/3}$ (Cackett et al. 2007). The high quality of the CCF lags detected in Section 3.1 allows us to test this prediction. We fitted the CCF lag spectrum, τ, as a function of wavelength, using the following functional form:

$$\tau = \tau_0 \left[\left(\frac{\lambda}{\lambda_0} \right)^\alpha - y_0 \right], \quad (1)$$

where τ_0 is the amplitude the power-law lag spectrum, α is the power-law index, $\lambda_0 = 1928$ Å is the reference wavelength (*UVW2* filter), and y_0 allows the model lag at λ_0 to differ from 0. Our fit uses only the UV and optical lags, omitting the X-ray/*UVW2* lag.

The CCF lag distributions are close to Gaussian, but with slight asymmetries. We averaged the low and high 1σ confidence intervals to use as our 1σ standard deviation. As with previous studies, we first fitted our delay spectrum to equation (1) for a fixed power-law index of $\alpha = 4/3$ and then fit with α as a free parameter, omitting the X-rays. In both cases, we find a consistent agreement with the standard accretion disc scaling prediction ($\tau \propto \lambda^{4/3}$), with a reduced $\chi^2/11 = 1.16$. In addition, when fitting for the slope, we find $\alpha = 0.93 \pm 0.39$, closer to a linear relation, with a reduced $\chi^2/10 = 1.17$. The full list of best-fitting parameters is shown in Table 2.

The high-quality X-ray light curve (and thus lag detection) and its clear connection between the optical and UV bands (see Section 3.2) allows us to better constrain the lag spectrum. In Fig. 4, we show the best fit to the CCF lags for a fixed power-law index of $\alpha = 4/3$ and then fit with α as a free parameter. Both fits overlap and produce consistent results for the size of the disc.

Previous studies have found CCF lag spectra suggesting that disc sizes are larger than expected by factors of $\sim$2–3. This *'too-big disc'* *problem* has been noted in a number of systems so far, e.g. Edelson et al. (2015, 2017, 2019), Fausnaugh et al. (2016), Cackett et al. (2018), and Pozo Nuñez et al. (2019). In Fig. 4, we show the lag spectrum prediction following Fausnaugh et al. (2016) and Pal et al. (2017):

$$\tau - \tau_0 = \frac{1}{c} \left(\frac{\lambda_0}{k} \right)^{4/3} \left(\frac{3\,G\,M\,\dot{M}}{8\,\pi\,\sigma} + \frac{(1-A)\,L_x\,H}{4\,\pi\,\sigma} \right)^{1/3}$$

$$\times \left[\left(\frac{\lambda}{\lambda_0} \right)^{4/3} - 1 \right], \quad (2)$$

where $k = 2.897 \times 10^{-3}$ mK is Wien's constant, σ is the Stefan–Boltzmann constant, $A = 0.2$ is the albedo, and $H = 6\,G\,M/c^2$ is the height of the illuminating X-ray source. We have used an Eddington ratio $L/L_{Edd} = 0.02$ (Vasudevan & Fabian 2009), to provide a direct
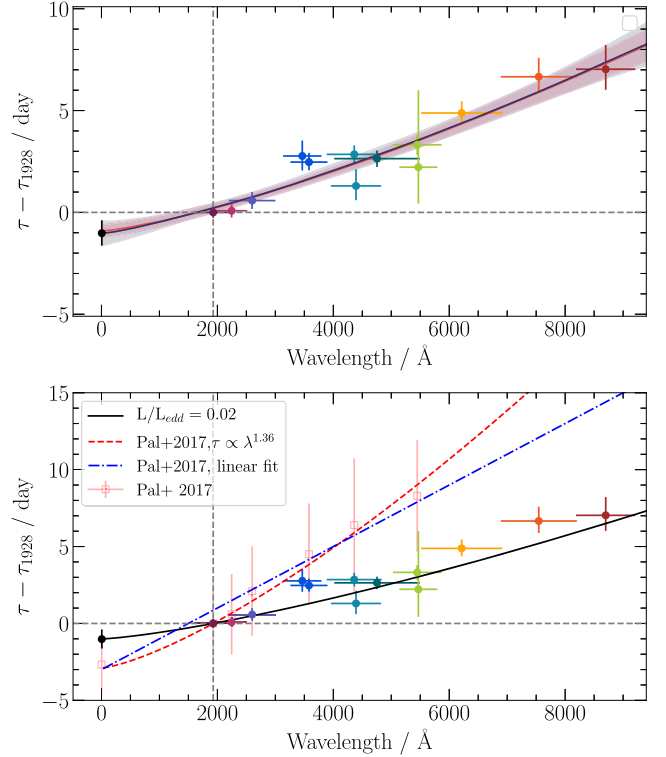

Figure 4. Inter-band lag spectrum of Fairall 9. Top panel: CCF lags as a function of wavelength for the *Swift* and LCO bands. All lags are measured with respect to the *Swift*/*UVW2* band. The best-fitting relation for the reprocessing model ($\tau \propto \lambda^{4/3}$) is shown as the red line and its 1σ error envelope is the shaded region. The black solid line and error envelope shows the fit when leaving the power-law index as a free parameter. Bottom panel: lag spectrum comparison between this work and the inter-band lags measured by Pal et al. (2017). We show their linear (blue) and exponential fits (red). The predicted lag spectrum for Fairall 9 is shown as the black line. This shows the clear need of IDRM campaigns to extract the lag spectrum with high accuracy.

comparison with the previous study of this source. We find a $\chi_\nu^2 = 13.049/12 = 1.087$ for the accretion disc prediction (omitting the *U* band and including the X-rays). In Pal et al. (2017), the observed lags using only *Swift*/UVOT provided evidence for a larger disc as shown in the bottom panel of Fig. 4, albeit a lower signal-to-noise ratio of their lag measurements. We note the strong disagreement between the accretion disc prediction and their lags measured, especially at long wavelengths. This demonstrates that IDRM, especially including long-wavelength ground-based measurements, can sharpen the tests of accretion disc theory predictions.
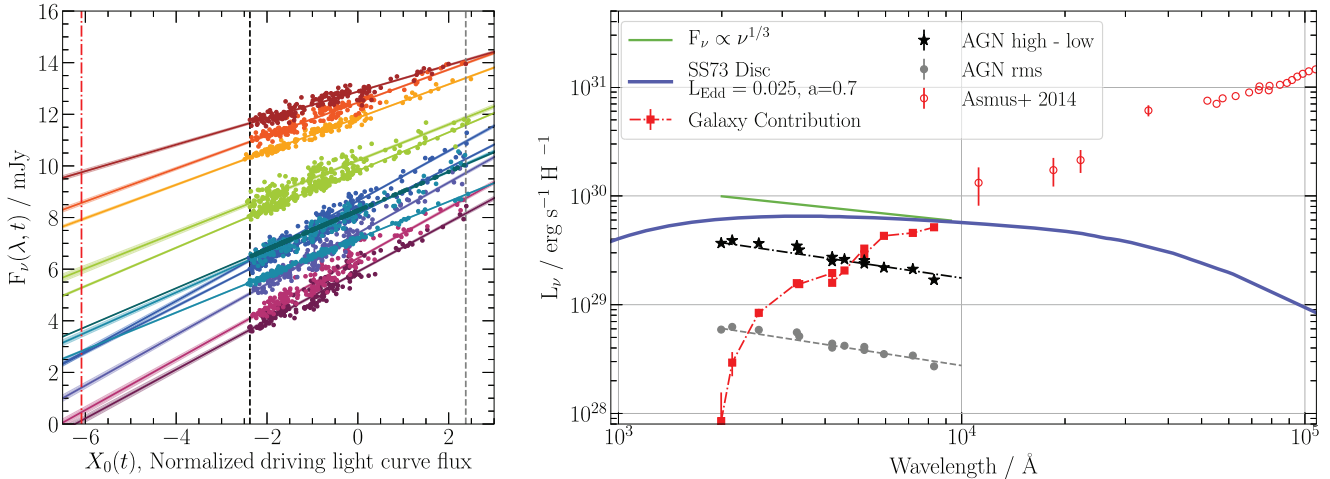
Figure 5. Left-hand panel: spectral decomposition of the variable component of Fairall 9 for all *Swift* and LCO light curves. The flux–flux plot uses the driving light curve obtained with CREAM. Vertical lines show the underlying galaxy contribution (red) as well as the AGN high (grey) and low (black) variable spectra. Right-hand panel: spectral energy distribution of the high-low (black) and rms (grey) variable component – AGN – as well as the constant component – galaxy + DCE (red). The mid- and far-IR measurements are shown as the open squares, taken from Asmus et al. (2014). All SEDs are corrected for extinction; see the text for details. The variable component are compared against a standard disc SED with an $L_{Edd} = 0.02$ and a BH spin, $a = 0.7$.

4.2 Spectral energy distribution

We calculated the fractional variability (F_{var}) as a function of wavelength (Rodríguez-Pascual et al. 1997; Vaughan et al. 2003). We followed the procedure described by Fausnaugh et al. (2016) and the results for each light curve are shown in Table 1. We find a decreasing value of F_{var} as a function of wavelength in the UV/optical bands. This is likely due at least in part to the contribution of the underlying galaxy, which has a redder spectral energy distribution (SED) than the variable AGN and will dilute the variability at longer wavelengths. Therefore, we expect that the shorter wavelengths trace closely the intrinsic variability of the AGN.

To test this, we constructed a flux–flux diagram, shown in the left-hand panel of Fig. 5, to decompose the spectrum between a variable (AGN) and a fixed component (host galaxy; e.g. Fausnaugh et al. 2016; Starkey et al. 2017; Cackett et al. 2020). We used the driving light curve $X(t)$ obtained in Section 3.2, which is normalized so that $\langle X \rangle = 0$ and $\langle X^2 \rangle = 1$. Then, we constructed a simple model for each light curve following:

$$F(\lambda) = C(\lambda) + S(\lambda) X(t), \qquad (3)$$

where the flux at each epoch t is a linear combination of $C(\lambda)$ and $S(\lambda)$. The correlation between the components throughout the luminosity range (noted as AGN low and AGN high) is well described by the linear model throughout the flux range of our sample, showing no evidence for curvature. Thus, extrapolating the linear model of the shortest wavelength until it reaches zero flux (to within 1σ), provides us with a lower limit on the galaxy and DCE contribution. Taking a vertical slice in this limit (dot dashed line in Fig. 5), we obtain the spectrum of the non-variable component of the light that we attribute to the underlying host galaxy. The de-reddened SED of the different components (low-state, high-state AGN and Galaxy spectrum) are explicitly shown in the bottom panel of Fig. 5. All flux values shown are de-reddened using $E(B - V) = 0.026 \pm 0.001$ (Schlafly & Finkbeiner 2011) and the Fitzpatrick (1999) model for Galactic dust extinction. As a sanity check, we have included the IR measurements (Asmus et al. 2013, 2014), shown as open circles in Fig. 5. These are consistent with the estimated galactic contribution. Using V band

as a proxy for the 5100 Å monochromatic flux, we find an average disc luminosity of $\log(\lambda F_\lambda / \mathrm{erg\,s^{-1}}) = 44.1$, slightly higher (0.18 dex) than that obtained from spectro-photometric decomposition $\log(L_{5100}/\mathrm{erg\,s^{-1}}) = 43.92$ (Bentz et al. 2013). This difference however is within the variability observed in this campaign and could explain the discrepancy.

The AGN spectrum shows a power-law slightly bluer than the canonical disc SED where $F_\nu \propto \nu^{1/3} \propto \lambda^{-1/3}$. The observed disc spectral index is $\alpha = 0.50 \pm 0.03$ for the variable component AGN using all bands and a shallower value when omitting U-band $\alpha = 0.45 \pm 0.05$ (shown as the black and grey lines in Fig. 5). It has been noted that the variable component in AGN is contaminated by other additional elements such as the BLR (Chelouche et al. 2019) and emission-line contribution. Thus, the observed variable SED may not be the pure accretion disc component and thus deviations/bias are expected. We show this explicitly in the right-hand panel of Fig. 5 where we display the predicted SED for a standard thin disc in Fairall 9. In general, the predicted SED is a factor of ~3 brighter than the average AGN spectrum, a characteristic previously observed in other systems, e.g. NGC 5548 (Starkey et al. 2017).

4.3 Diffuse continuum emission from the BLR

The spectral decomposition and the lag spectrum both show evidence for deviation from simple power laws. In particular, the U-band excess has been previously observed in the *Swift* sample of five AGN (Edelson et al. 2019) and more clearly shown in the *HST* data of NGC 4593 (Cackett et al. 2018) and NGC 5548 (Fausnaugh et al. 2016). Furthermore, non-disc contributions to the optical reverberation signal of Mrk 279 across all continuum bands are needed to fully account for the variability observed (Chelouche et al. 2019). These discrepancies have been interpreted as the contribution from the DCE of the BLR, due to free–free and free–bound hydrogen transitions (e.g. Korista & Goad 2001). The imprint of the BLR in the lag spectrum is particularly reflected as longer lags towards the Balmer (3646 Å) and Paschen (8204 Å) edges in the optical range (Lawther et al. 2018; Korista & Goad 2019; Netzer 2020). For local AGN, such longer lags should be particularly noticeable in U and
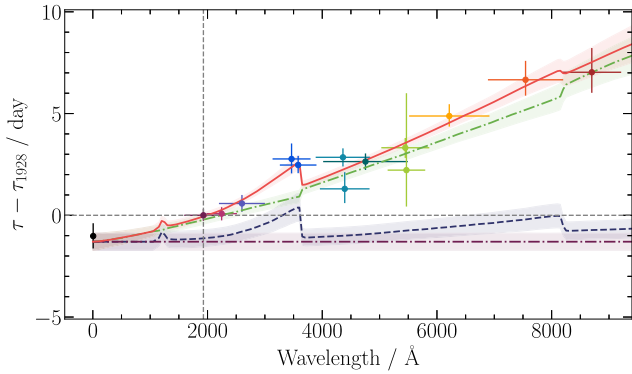
Figure 6. Lag spectrum fit using a scaled version of the DCE model for NGC 5548 (blue dashed line), the accretion disc model represented by a power law (green dashed line). The UVW2 offset is shown as the straight purple line. The envelope in each line represent the 1σ confidence intervals.

i bands, respectively (where redshift is not large enough to move the edges out of the filter passbands).

The *U*-band excess is observed in data from both *Swift* and LCO during this first year of Fairall 9 monitoring. The excess *U*-band lag relative to the $\tau \propto \lambda^{4/3}$ relation is quite small, ~ 20 per cent, which limits the extent to which reprocessing in the BLR can contribute to the observed variations. In addition to the lag spectrum, the variable component of the SED also presents evidence for the Balmer edge and marginal evidence in the Paschen edge in emission.

We present here a physically motivated fit to the observed lag spectrum based on the previous work of Korista & Goad (2019), who modelled the well-studied case of NGC 5548. We use the DCE lag spectrum contribution from the BLR (top panel in their fig. 6) and scale this as recommended to reflect the luminosity difference between NGC 5548 and Fairall 9, hence the size of the BLR, following the radius–luminosity relation $R_{\mathrm{BLR}} \propto L^{1/2}$, where the ratio between their luminosity is $(L_{\mathrm{AGN}}/L_{\mathrm{NGC\,5548}}) = (0.02/0.1)$. We then mix the disc lag spectrum $\tau_{\mathrm{disc}}(\lambda)$ and the luminosity-scaled DCE lag spectrum $\tau_{\mathrm{DCE}}(\lambda)$, weighted at each wavelength by their relative fluxes. For NGC 5548, the wavelength-dependent flux ratio $f(\lambda)$ between the DCE and the disc emission is given by Korista & Goad (2019, see their fig. 9). Therefore, the lag spectrum is defined by the following parametrization:

$$\tau(\lambda) - \tau(\lambda_0) = \frac{\tau_{\mathrm{disc}}\,(\lambda/\lambda_0)^{\alpha} + \tau_{\mathrm{DCE}}(\lambda)\,B\,f(\lambda)}{1 + B f(\lambda)} - \tau_0, \qquad (4)$$

where τ_{disc} is the disc continuum lag at $\lambda = \lambda_0$, α is the power-law index of the disc lag spectrum, $\tau_{\mathrm{DCE}}(\lambda)$ is the DCE lag spectrum of NGC 5548, scaled by $L^{1/2}$ to the luminosity of Fairall 9, $f(\lambda)$ is the flux ratio in NGC 5548 of the DCE spectrum to the disc spectrum, B is a dilution factor, allowing the DCE contribution to be stronger or weaker in Fairall 9 than in NGC 5548, and τ_0 is the total (disc + DCE) lag at the reference wavelength, $\lambda_0 = 1928$ Å for our CCF lags.

Our four-parameter model fits for α, τ_{disc}, B, and τ_0, with $\tau_{\mathrm{DCE}}(\lambda)$ and $f(\lambda)$ taken from Korista & Goad (2019). We used an MCMC procedure to sample the posterior parameter distribution using EMCEE (Foreman-Mackey et al. 2013), using uniform priors for all parameters. We find marginalized posterior distributions for each parameters to be $\alpha = 1.39 \pm 0.27$, $\tau_{\mathrm{disc}} = 1.08 \pm 0.44$, $B = 0.26 \pm 0.12$, and $\tau_0 = 1.31 \pm 0.48$ d. The resulting fit, and contributions from each component with their respective 1σ error envelope, are shown in Fig. 6. Joint and marginal posterior distributions for the parameters are shown in Fig. D1.

Notice that for this disc + DCE model of the lag spectrum of Fairall 9, the DCE enhances lags near the Balmer and Paschen edges without greatly influencing the power-law disc lag spectrum. Thus, the simpler procedure of omitting the *U*-band lag when fitting a power-law lag spectrum seems to be justified (as suggested by Korista & Goad 2001). If this is true also for AGN that have measured disc continuum lags larger than expected, then the DCE component may not cure the problem.

The previous analysis shows that, qualitatively, the inclusion of the DCE provides a better representation of the measured lag spectrum. In particular, our parametrization uses a simple scaling of AGN NGC 5548 as a proxy for the DCE contribution. This assumes that the wavelength dependence remains the same for Fairall 9, while the main difference lies on the fractional contribution (i.e. scaling). However, changes in the ionizing luminosity between these two systems can give rise to significant changes in both of aspects. For example, specific differences in the ionizing spectral shape can provide changes in the DCE contribution by a factor of ~ 2 (Netzer 2020). A detailed modelling of the DCE in Fairall 9 and their effect on the lag spectrum and SED is beyond the scope of this paper and will be deferred to a future analysis including additional spectroscopic and photometric monitoring over the 2-yr Key Project.

4.4 Fast and slow variations

Long-term optical correlations have been observed in several AGN (e.g. Uttley et al. 2003; Breedt et al. 2009). These studies concluded that the X-ray reprocessing was not the sole driver of variability. The decomposition of the driving light curve from CREAM (see Fig. 3) suggests that the observed variability arises from rapid variations, likely due to reprocessing of X-rays, and slower variations on longer time-scales (>100 d). To quantify this slow component, we use a quadratic fit to detrend the light curves, as performed in Section 3.1. Since this fit may carry temporal information, we have parametrized it as follows to characterize its evolution:

$$F_{\nu}(\lambda, t) = F_0(\lambda) + \Delta F(\lambda) \left(\frac{t - t_0(\lambda)}{100\,\mathrm{d}} \right)^2, \qquad (5)$$

where F_0 is the flux at the minimum of the parabola, which occurs at time t_0, and ΔF is the flux rise 100 d before or after the minimum. In the left-hand panel of Fig. 7, we show the full decomposition of *Swift* and LCO light curves. The fast variations (residuals after detrending) have a red lag spectrum. The lag increases with wavelength, as obtained from the CCF lags (see Section 3.1) and we reproduce in the upper right-hand panel of Fig. 7. For the parabolic fits, the times of minimum, $t_0(\lambda)$ (shown as a diamond on each light curve in Fig. 7) decrease with wavelength. Using the *UVW2* filter as reference, we show this distribution of these minima in the lower right-hand panel of Fig. 7. While the uncertainties are larger than the reverberation signal, the trend is clear for most wavelengths despite the flattening at the two longest ones. We explore possible origins of this component in the following section.

This opposite lag signal in the slow component could be interpreted as accretion-rate fluctuations propagating inwards through the accretion disc, from cooler to hotter regions, on the local viscous time-scale (e.g. Lyubarskii 1997; Arévalo et al. 2008). This would translate to an observable wavelength-dependent lag where the lower energies lead the higher ones, such as the trend shown in Fig. 7. However, the ~ 10-d time-scale indicated by the time shifts in the minima of the parabolic fits is rather shorter than the viscous time-scale expected for classical thin discs. However, this delay is not simply the propagation time of accretion fluctuations, but propagation time convolved with
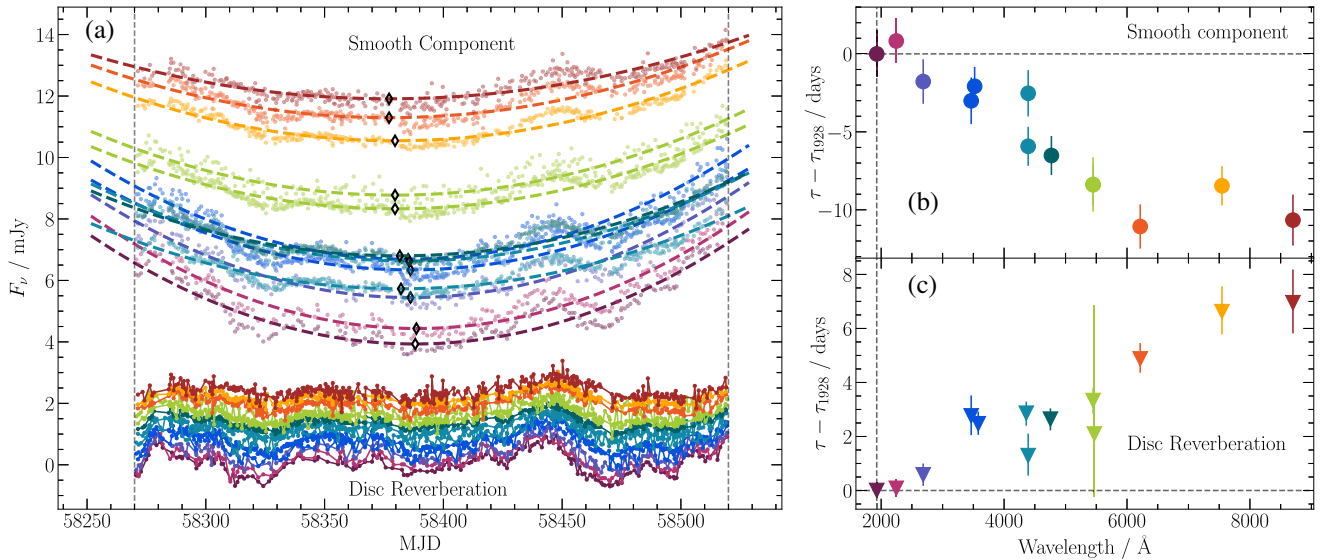
Figure 7. Identification of two variable components in the year 1 data of Fairall 9. Panel (a) shows the LCO and *Swift* light curves, colour coded by wavelength, with their respective parabolic fit as the dashed line. The minimum of each parabola is shown as a black diamond. Note that these progress to earlier times in the redder light curves. Residual light curves (data minus parabolic fit) are shown in the bottom of the panel, with an arbitrary shift for display purposes. Note the peak near MJD 58450 shifting to later times in the redder light curves. Panel (b) shows the blue lag spectrum of the slow variations, as measured by the minimum of the quadratic fit used to detrend each individual light curve. We show the difference between these minima relative to the UVW2 band. Panel (c) shows the red lag spectrum of the fast variations, as measured from the CCF analysis (see Section 3.1) of the residual light curves. These lags increasing with wavelength are attributed to light-travel times for X-rays reprocessed in small hot and later in large cool annuli of the accretion disc.

the weighted radial emission profile in each band. For any given radius, the disc will emit over a range of wavelengths, which will further suppress the lag, since one is unable to map one particular filter/band to a narrow range of radii.

Moreover, the variable emission observed at any given band may carry information at different time-scales, which trace different average radii on the disc (e.g. Arévalo et al. 2008). For example, the inner radii of the disc may only produce a small fraction of optical light (due to smaller centrally concentrated regions closer to the BH) and will mostly vary (slowly) due to accretion fluctuations propagating at a viscous time-scale. While the outer radii may produce a larger fraction of optical light which is relatively constant (since the time-scales are longer farther out), a fraction of its light will vary due to X-ray reprocessing. Thus, the fast variability may come from larger radii than the slow variability (hence the lags can be similar but with different sign). In BH X-ray binaries, there is strong evidence that thermal emission from the innermost parts of the optically thick disc also shows strong intrinsic variability (at lower energies) that leads the Comptonized (higher energy) emission by time delays much longer than light-travel times (Uttley et al. 2011). In particular, they observe lags of ∼0.1 s on seconds time-scales, which, scaled for Fairall 9, would represent few tens of days lead on year time-scales.

An alternative way to interpret the parabolic fits is that a change in colour of the slow component's SED can mimic time-delayed variations. If the SED is slightly redder at the start of our observations and bluer near the end, the minimum of the parabola will be later in the blue and earlier in the red, mimicking a time delay increasing from red to blue. In this interpretation, the relevant time-scale is not the 10-d shift of the minimum of the parabola, but the much longer time over which the SED colour changes.

Multiyear monitoring of Fairall 9 should clarify which if either of these interpretations is correct and show the robustness the

detection of the slow component. The simple parabolic fit, while informative in this particular year of monitoring, is obviously not viable as a long-term description of the slow component. This issue will require to fully model the underlying background contribution as a smooth polynomial or as an independent light curve (with different PSD as the reverberation signal). In addition, if these components have indeed opposite lag directions, the 'average' lag measured without any detrending (that for Fairall 9 removes the slow component) might produce bias lag measurements. This could potentially affect all reverberation experiments if not considered. Our continued monitoring of Fairall 9 will provide a more detailed record of the slow and fast variations, allowing for a more secure separation and characterization of the fast and slow components over a longer time span and allow us to understand the correlations between them.

5 CONCLUSIONS

We report analysis of the first year of X-ray, UV, and optical monitoring of Fairall 9 with the *Swift* Observatory and the ground-based LCO robotic telescope network. Sustained photometric monitoring of the X-rays and 13 UV/optical bands was achieved with a 1-d cadence by *Swift* and subday cadence by LCO.

The main results of our analysis of the spectral variations may be summarized as follows:

(1) The observed UV and optical light curves can be decomposed into slow variations that we model with a parabola, and faster variations that correlate with the observed X-ray variations.

(2) Cross-correlation lag measurements for the faster variations, measured relative to those in the *Swift* UVW2 band, increase with wavelength with a power-law index $\alpha = 1.26 \pm 0.23$, compatible with the $\tau \propto \lambda^{4/3}$ prediction of accretion disc theory.

(3) The lag spectrum relative to *UVW2* increases from -1.0 ± 0.6 for the X-rays to 7.0 ± 1.2 d at longest wavelength z_s band, compatible with the prediction of accretion disc theory for the source Eddington ratio $L/L_{edd} = 0.02$.

(4) Decomposing the data into mean and variable components, we isolate the disc spectrum as the variable component and find that its power-law spectral index, 0.5 ± 0.02, is slightly bluer than the standard accretion disc prediction of $F_\nu \propto \nu^{1/3}$.

(5) Evidence for a Balmer jump in emission is evident in both the delay spectrum and the disc flux spectrum, with a small ~ 20 per cent amplitude relative to the power law. This places limits on the contribution of diffuse bound-free continuum emission from reprocessing in the BLR.

(6) The slowly varying component shows a blue lag spectrum, with lags decreasing with wavelength. These may be indicative of variations in the accretion flow in the disc. However, the origin of the slow component is uncertain but should be clarified through our continued monitoring of Fairall 9.

ACKNOWLEDGEMENTS

DATA AVAILABILITY

The raw data sets were derived from sources in the public domain: LCO archive https://archive.lco.global and *Swift* archive https://www.swift.ac.uk/swift_live. The inter-calibrated light curves and *Swift* detector maps are available in Zenodo, at https://dx.doi.org/10.5281/zenodo.3956577.

REFERENCES

Arévalo P., Uttley P., Kaspi S., Breedt E., Lira P., McHardy I. M., 2008, MNRAS, 389, 1479

Asmus D., Hoenig S., Gandhi P., Smette A., Duschl W., 2013, Subarcsecond Mid-infrared Atlas of Local AGN. Available at: https://dc.zah.uni-heidelberg.de/sasmirala/q/cone/info

Asmus D., Hönig S. F., Gandhi P., Smette A., Duschl W. J., 2014, MNRAS, 439, 1648

Astropy Collaboration et al., 2013, A&A, 558, A33

Bentz M. C., Katz S., 2015, PASP, 127, 67

Bentz M. C. et al., 2013, ApJ, 767, 149

Bertin E., Arnouts S., 1996, A&AS, 117, 393

Blackburn J. K., 1995, in Hayes J. J. E., Payne H. E., Shaw R. W., eds, ASP Conf. Ser. Vol. 77, Astronomical Data Analysis Software and Systems IV. Astron. Soc. Pac., San Francisco, p. 367

Blandford R. D., McKee C. F., 1982, ApJ, 255, 419

Brandt W. N., Alexander D. M., 2015, A&AR, 23, 1

Breedt E. et al., 2009, MNRAS, 394, 427

Breeveld A. A., Landsman W., Holland S. T., Roming P., Kuin N. P. M., Page M. J., 2011, in McEnery J. E., Racusin J. L., Gehrels N., eds, AIP Conf. Ser. Vol. 1358, Gamma Ray Bursts 2010. Am. Inst. Phys., New York, p. 373

Brown T. M. et al., 2013, PASP, 125, 1031

Burrows D. N. et al., 2005, Space Sci. Rev., 120, 165

Cackett E. M., Horne K., Winkler H., 2007, MNRAS, 380, 669

Cackett E. M., Chiang C.-Y., McHardy I., Edelson R., Goad M. R., Horne K., Korista K. T., 2018, ApJ, 857, 53

Cackett E. M. et al., 2020, ApJ, 896, 12

Chelouche D., Pozo Nuñez F., Kaspi S., 2019, Nat. Astron., 3, 251

Degenaar N., Miller J. M., Kennea J., Gehrels N., Reynolds M. T., Wijnands R., 2013, ApJ, 769, 155

De Rosa G. et al., 2015, ApJ, 806, 128

Edelson R. et al., 2015, ApJ, 806, 129

Edelson R. et al., 2017, ApJ, 840, 41

Edelson R. et al., 2019, ApJ, 870, 123

Emmanoulopoulos D., Papadakis I. E., McHardy I. M., Nicastro F., Bianchi S., Arévalo P., 2011, MNRAS, 415, 1895

Evans P. A. et al., 2009, MNRAS, 397, 1177

Event Horizon Telescope Collaboration et al., 2019, ApJ, 875, L1

Fabian A. C., 2012, ARA&A, 50, 455

Fairall A. P., 1977, MNRAS, 180, 391

Fausnaugh M. M. et al., 2016, ApJ, 821, 56

Fitzpatrick E. L., 1999, PASP, 111, 63

Foreman-Mackey D., 2016, J. Open Source Softw., 1, 24

Foreman-Mackey D., Hogg D. W., Lang D., Goodman J., 2013, PASP, 125, 306

Gardner E., Done C., 2017, MNRAS, 470, 3591

Gaskell C. M., Peterson B. M., 1987, ApJS, 65, 1

Gehrels N. et al., 2004, ApJ, 611, 1005

Gravity Collaboration et al., 2018, Nature, 563, 657

Grier C. J. et al., 2017, ApJ, 851, 21

Hawley S. A., Phillips M. M., 1978, ApJ, 225, 780

Henden A. A., Levine S., Terrell D., Welch D. L., Munari U., Kloppenborg B. K., 2018, AAS Meeting Abstracts #232, p. 223.06

Hunter J. D., 2007, Comput. Sci. Eng., 9, 90

Korista K. T., Goad M. R., 2001, ApJ, 553, 695

Korista K. T., Goad M. R., 2019, MNRAS, 489, 5284

Lawther D., Goad M. R., Korista K. T., Ulrich O., Vestergaard M., 2018, MNRAS, 481, 533

Lohfink A. M., Reynolds C. S., Vasudevan R., Mushotzky R. F., Miller N. A., 2014, ApJ, 788, 10

Lohfink A. M. et al., 2016, ApJ, 821, 11

Lynden-Bell D., 1969, Nature, 223, 690

Lyubarskii Y. E., 1997, MNRAS, 292, 679

McCully C. et al., 2018, SPIE Conf. Ser. Vol. 10707, Software and Cyberinfrastructure for Astronomy V. SPIE, Bellingham, p. 107070K

McHardy I. M. et al., 2018, MNRAS, 480, 2881

Netzer H., 2020, MNRAS, 494, 1611

Pal M., Dewangan G. C., Connolly S. D., Misra R., 2017, MNRAS, 466, 1777

Peterson B. M., Wanders I., Horne K., Collier S., Alexander T., Kaspi S., Maoz D., 1998, PASP, 110, 660

Peterson B. M. et al., 2004, ApJ, 613, 682

Poole T. S. et al., 2008, MNRAS, 383, 627

Pooley D., Blackburne J. A., Rappaport S., Schechter P. L., 2007, ApJ, 661, 19

Pozo Nuñez F. et al., 2019, MNRAS, 490, 3936

Ricker G. R., 1978, Nature, 271, 334

Rodríguez-Pascual P. M. et al., 1997, ApJS, 110, 9

Roming P. W. A. et al., 2005, Space Sci. Rev., 120, 95

Salpeter E. E., 1964, ApJ, 140, 796

Schlafly E. F., Finkbeiner D. P., 2011, ApJ, 737, 103

Shakura N. I., Sunyaev R. A., 1973, A&A, 500, 33

Siegel M. H., Porterfield B. L., Balzer B. G., Hagen L. M. Z., 2015, AJ, 150, 129

Starkey D. A., Horne K., Villforth C., 2016, MNRAS, 456, 1960

Starkey D. et al., 2017, ApJ, 835, 65

Stetson P. B., 1987, PASP, 99, 191

Uttley P., Edelson R., McHardy I. M., Peterson B. M., Markowitz A., 2003, ApJ, 584, L53

Uttley P., Wilkinson T., Cassatella P., Wilms J., Pottschmidt K., Hanke M., Böck M., 2011, MNRAS, 414, L60

Valenti S. et al., 2016, MNRAS, 459, 3939

Vasudevan R. V., Fabian A. C., 2009, MNRAS, 392, 1124

Vaughan S., Edelson R., Warwick R. S., Uttley P., 2003, MNRAS, 345, 1271

Wheeler D. J., Chambers D. S., 1992, Understanding Statistical Process Control, 2nd edn. SPC Press, Knoxville, Tenn.

White R. J., Peterson B. M., 1994, PASP, 106, 879

Zel'dovich Y. B., 1964, Sov. Phys. Dokl., 9, 195

APPENDIX A: A TOOL FOR FILTERING 'DROPOUTS' FROM *SWIFT* UVOT DATA

A1 Detector map from Galactic Centre data

As first noted by Edelson et al. (2015), *Swift* UVOT light curves exhibit occasional 'dropouts': fluxes that are anomalously low relative to the nearby data and apparently not intrinsic to the source.

Our earlier work indicated this is due to localized low-sensitivity regions in the UVOT detector plane. We developed a methodology that used these dropouts in the AGN light curves to map and mask out these problematic regions (e.g Edelson et al. 2015, 2017, 2019, for details). However, because these observations only sparsely sample the detector plane, masks defined from them are optimized only for correcting the light curve of the target AGN. Here we develop more detailed, generally applicable maps of the problematic detector regions and apply them to mask the Fairall 9 data, as discussed below.

The Galactic Centre (Sgr A∗) has been monitored with near-daily observations since early in the *Swift* mission (Degenaar et al. 2013). Each observation provides numerous sensitivity measurements scattered across the full UVOT field of view (FoV) due to the high stellar density of this field. This provides a near-ideal data set for this endeavour, as the FoV is sampled densely and relatively uniformly, as opposed to the AGN data, which sparsely measure only a portion of the detector plane.

Sgr A∗ field star data were taken from 3202 observations from 2006 Febraury 6 through 2018 April 22. Three hundred fifty-five field stars were tracked and their fluxes measured whenever they fell within the UVOT FoV, yielding a total of 531 132 measurements. These data were screened and processed following the same procedures applied to the Fairall 9 data (Section 2.2). Additional screening eliminated any data points with large coincidence loss correction factors or flux uncertainties. Light curves for each star in each filter are modelled by fitting a second-order polynomial to the neighbouring data points within a sliding window centred upon each measurement, iteratively rejecting outliers. Final model values are recorded only for measurements that retain at least nine neighbours that constrain the light-curve model without extrapolation. To ensure model quality, light curves are rejected if they included too few data points (<50 after screening), do not fully represent variability in the
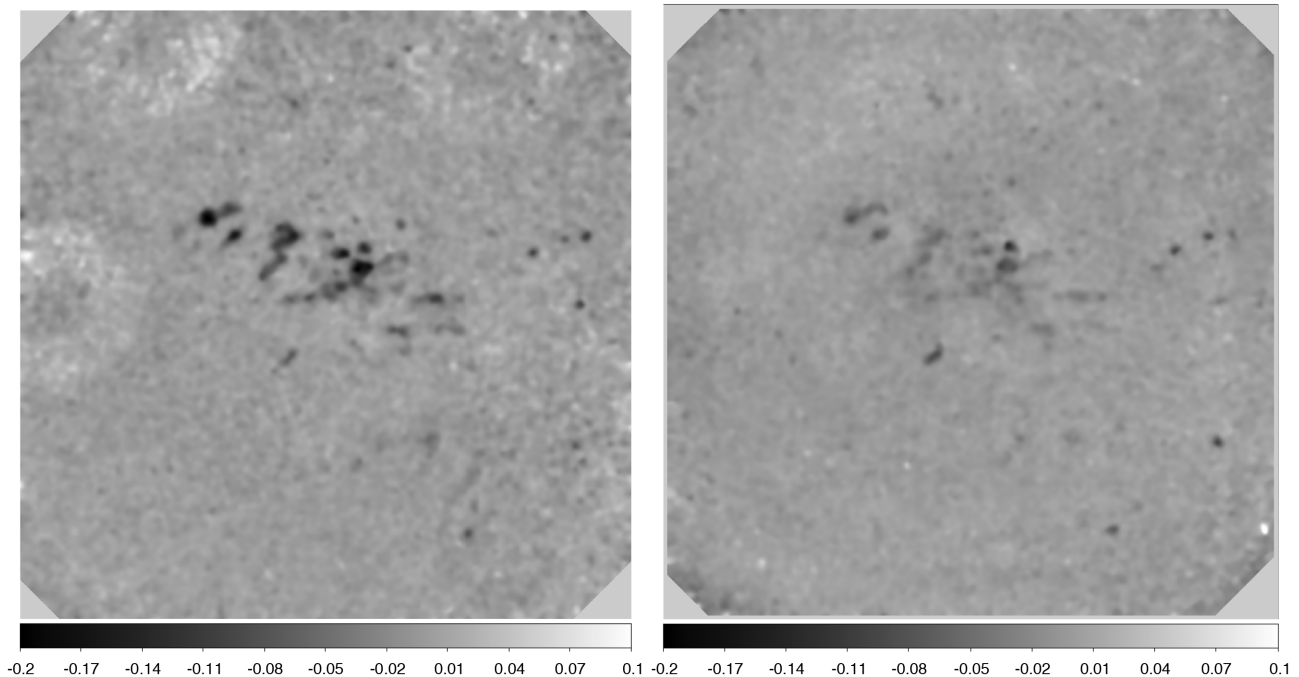

Figure A1. Heat maps combining data from all UV filters (left-hand panel) and *U* filter data (right-hand panel), both smoothed with a 5-arcsec kernel. These are the final maps used to define the detector masks for the UV and optical bands. The grey-scale ranges of the panels are matched, showing that the effect of the low sensitivity regions is greater in the UV than in the optical. The primary low-sensitivity (dark) regions in the two maps line up, but the most extreme regions in one map are not the darkest regions in the other.
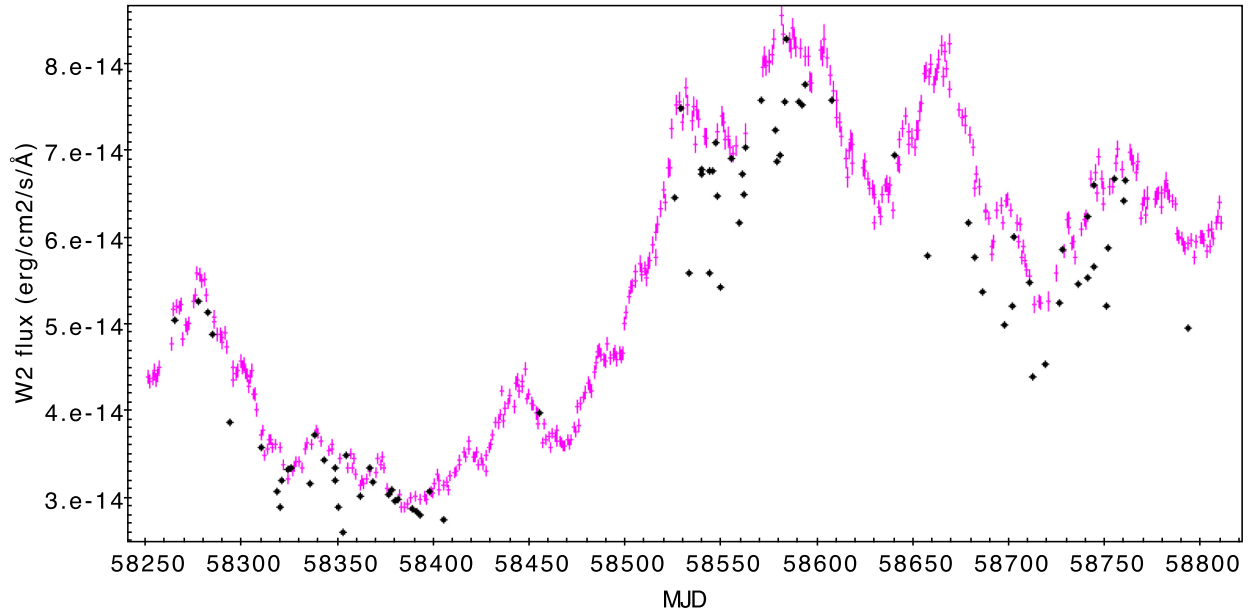
Figure A2. Fairall 9 light curve in *W2*. The filled, coloured points with error bars are the final sample of *W2* measurements while the smaller black points are ones that pass all other screening but are flagged by the mask of low-sensitivity regions.

data, or if the median uncertainty of data used to define the light curve is large. This eliminates all *B* and *V* light curves, as there are few Sgr A∗ observations in these filters.

To generate UVOT sensitivity maps, the fractional flux differences between measurements and light-curve models are projected on to the detector plane. The flux deviations are evaluated for a final sample of 136 718 data points with robust light-curve model values and small measurement uncertainties. Preliminary detector coordinates for each measurement are obtained from the centroids of Gaussians fitted to the stars in raw images. These coordinates are then corrected for offsets due to shift-and-add (S&A) processing. The median of the S&A offsets applied to each image (which is typically 8–10 arcsec and can be determined from log files) is subtracted from the fitted coordinates to determine the detector position that most strongly influences each measurement.

The final sensitivity maps are produced by assigning to each 1-arcsec pixel (after two times binning) the average of all nearby deviation measurements, weighted by distance from the pixel centre. By applying Gaussian weighting functions with different kernel sizes, sets of maps are generated with varying amounts of smoothing. Such sets are generated for each filter. In addition, multifilter maps that combine W2 and M2 or all three UV maps are generated to improve the sampling statistics, as there are strong similarities between these maps and fewer light-curve deviation measurements are available in the UV filters. Sample maps are shown in Fig. A1.

Field stars from the AGN IDRM campaigns are used to test the heat maps. These provide a pool of independent measurements in six UVOT filters, with high-cadence monitoring and spatial sampling that spans the FoV. The same procedure is followed to model the stellar light curves and select the highest quality data to use for measuring deviations from the models. The test pool is limited to data within 4.5 arcmin of the FoV centre, as this is where 95 per cent of planned targets fall. The final set of test data includes 1200–1600 measurements in each UV filter and 2900–5100 in the optical filters. The flux deviations measured from these data correlate with the corresponding heat map values, thereby corroborating the mapping of detector sensitivity variations.

The strengths of these correlations are used to make the final heat map selection. In each UV filter, the deviations are found to correlate most strongly with the maps that combine Sag A∗ deviations in all three UV filters, whereas the optical measurements correlate better with the heat map defined from *U*-filter data. As for the smoothing kernel choice, the correlation strength peaks with a kernel size of 5 arcsec for the UV filters and 4 arcsec in the optical bands. However, the correlation coefficient differences between these kernels are mostly just a few thousandths, so a 5-arcsec kernel is selected for all maps to provide consistency across all filters. The selected maps, shown in Fig. A1, will be made available for download in Zenodo.

Masks are defined to screen out data most strongly affected by regions of low sensitivity, as indicated by the heat maps. While the exact amplitude of the effect depends upon the filter and smoothing dilutes gradients and structure in the maps, thresholds may be used to identify where the effect is strongest. The thresholds are set by comparing the test pool deviation measurements to the corresponding heat map values at their detector locations. Masking thresholds are set at the highest heat map value for which 80 per cent of the test pool deviations are negative. The masks for *W2*, *M2*, and *W1* are defined using threshold values of −0.015 70, −0.011 52, and −0.011 00 (respectively) with the UV heat map, while the masks for *U*, *B*, and *V* apply thresholds of −0.013 33, 0.026 41, and −0.029 00 to the optical heat map. These masks can be downloaded as a single FITS file from Zenodo. To apply them, albeit without accounting for S&A offsets in the data (as of 2020 June), follow the UVOT small-scale sensitivity check procedure,[7] substituting the new masks as the LSSFILE parameter passed to the FTOOLS UVOT measurement routines (e.g. UVOTSOURCE).

Fig. A2 shows the result when the *W2* mask is applied to the Fairall 9 light curve: All clear dropouts and many other low data points are screened out, while very few screened points are consistent with neighbouring points in the light curve. In total, 16.5 per cent of

---

[7]This procedure is described by the UVOT team on their Small Scale Sensitivity page.

the measurements are masked (82 out of 497). When the same mask is applied to the *W2* test pool data, 13.7 per cent (222 out of 1622) data points are screened. The difference in percentage is due to the spatial distribution of measurements, as the test pool data are spread fairly evenly across the centre of the FoV whereas pointed observations at a single target over consecutive days tend to fall in clusters on the detector. This spatial correlation is what causes the masked data points to be concentrated in specific time periods across the light curve.

A2 Detector map from M3 data

As an additional independent check of our updated dropout filter mask, we reprocessed the photometry of the globular cluster M3 (NGC 5272) presented in Siegel et al. (2015). We produced DAOPHOT (Stetson 1987) point-source photometry from the *raw* UVM2 spacecraft images, which are corrected for instrumental effects but not translated to a sky reference frame. This means that detections are in CCD pixel coordinates. After performing PSF photometry, we matched all the frames, calculated variability for each point source and searched the data base, comprising 285 000 photometric measures of 5539 stars on 72 individual frames, for drops in flux greater than three times the photometric uncertainty.

This analysis is complicated by M3 being host to many RR Lyrae variable stars, which tend to dominate the UV detections. Indeed, the data come from a survey designed to identify and characterize RR Lyrae stars, which have very large pulsations in the UV (Siegel et al. 2015, and references therein). This tends to produce both more photometric outliers, larger photometric outliers, and a bias toward positive residuals (i.e. detections of RR Lyrae when they are brighter than their mean flux).

None the less, we find that the M3 analysis yields results that are very similar to those obtained for the Galactic Centre The M3 data reveal a distinct clustering of low-flux measurements beginning slightly above the chip centre and extending toward the upper right portion of the chip. The amplitude of the dropouts tend to be significantly larger than seen in the heat maps (20–50 per cent) due to a combination of factors: The M3 deviation measurements combine intrinsic variability with detector bias, while the values in the heat map are diluted by measurements in the *UVW1* filter, which have smaller deviation amplitudes and contribute the largest fraction of data in the map. When considering just Sgr A* measurements in the *UVM2* band, the largest flux deviation measured is 33.4 per cent. A more detailed analysis will fit intrinsically variable light curves and measure deviation from them. However, this preliminary analysis does confirm both methods and that this dropout effect is seen in point source photometry generated from all UVOT images, even photometry generated a *local* solution to the background sky level.

APPENDIX B: LIGHT CURVES OF FAIRALL 9

Here we present the format for all the light curves used in this paper. The *Swift*/UVOT UV filters are noted as $UVW2 = W2$, $UVM2 = M2$, and $UVW1 = W1$. The optical filters names are provided with

Table B1. Light-curve file format for year 1 of the IDRM of Fairall 9. The errorbars represent the 1σ confidence interval.

Filter	Time (MJD)	Flux (mJy)	Error (mJy)
W2	58251.65954	5.454	0.089
W2	58252.45592	5.383	0.087
W2	58253.86214	5.430	0.084
W2	58254.58299	5.548	0.090
W2	58255.51821	5.405	0.093
...	...	...	...
zL	58522.04347	14.075	0.153
zL	58523.04287	14.143	0.153
zL	58523.43402	13.757	0.154
zL	58524.43295	14.113	0.154
zL	58529.03947	14.450	0.153

Notes. The light curves show the inter-calibrated light curves, as described in Section 2.3.1. This table is available in a machine-readable format.

Table B2. Systematic error determination for the LCO light curves.

Filter	Mean error (mJy)	Added Error (mJy)	Error ratio
u'	0.032	0.183	5.76
B	0.016	0.078	4.86
g'	0.013	0.056	4.34
V	0.019	0.073	3.81
r'	0.020	0.065	3.27
i'	0.025	0.095	3.83
z_s	0.030	0.152	5.03

Notes. The mean error shows the values of the uncertainties from our data reduction pipeline. The Added Error shows the values obtained in Section 2.3.1. These were added to every data point in quadrature. The last column shows the ratio between the original average error bars and those after the inter-calibration process.

two letters, where the first one corresponds to the filter name and the second one to the observatory. For example, BS corresponds to the *B* band in *Swift* while BL to the *B* band in LCO. The full data set is available in a machine-readable format.

The calibrated errors for the LCO light curves were obtained by adding in quadrature the additional scatter obtained in Section 2.3.1. These values for each filter are presented in Table B2. In general, the systematic uncertainty is a factor of ∼3–5 larger than the original error bars.

APPENDIX C: CREAM FIT LIGHT CURVES TO A FACE-ON ACCRETION DISC

Figs C1 and C2 show the best fit from CREAM to every *Swift* and LCO band.
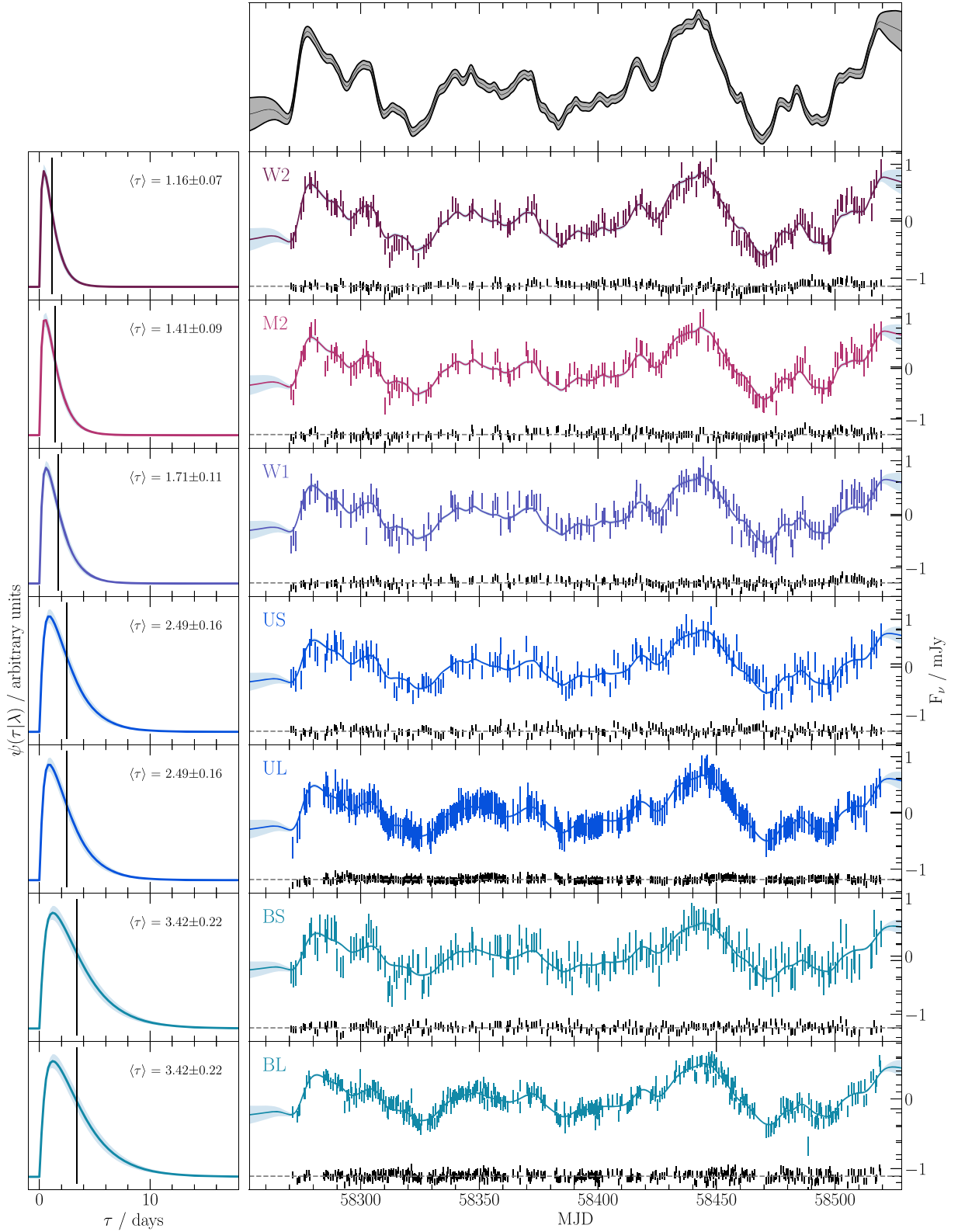
Figure C1. Reverberation model fit with CREAM to a face-on accretion disc and a $T \propto R^{-3/4}$ temperature profile for Fairall 9. The top panel shows the inferred driving light curve. The left-hand panels show the delay distribution for each band. The right-hand panel shows the photometry after the quadratic detrend and the best fit. The black points around the dotted grey line show the residuals. All grey envelopes represent the 1σ confidence interval.
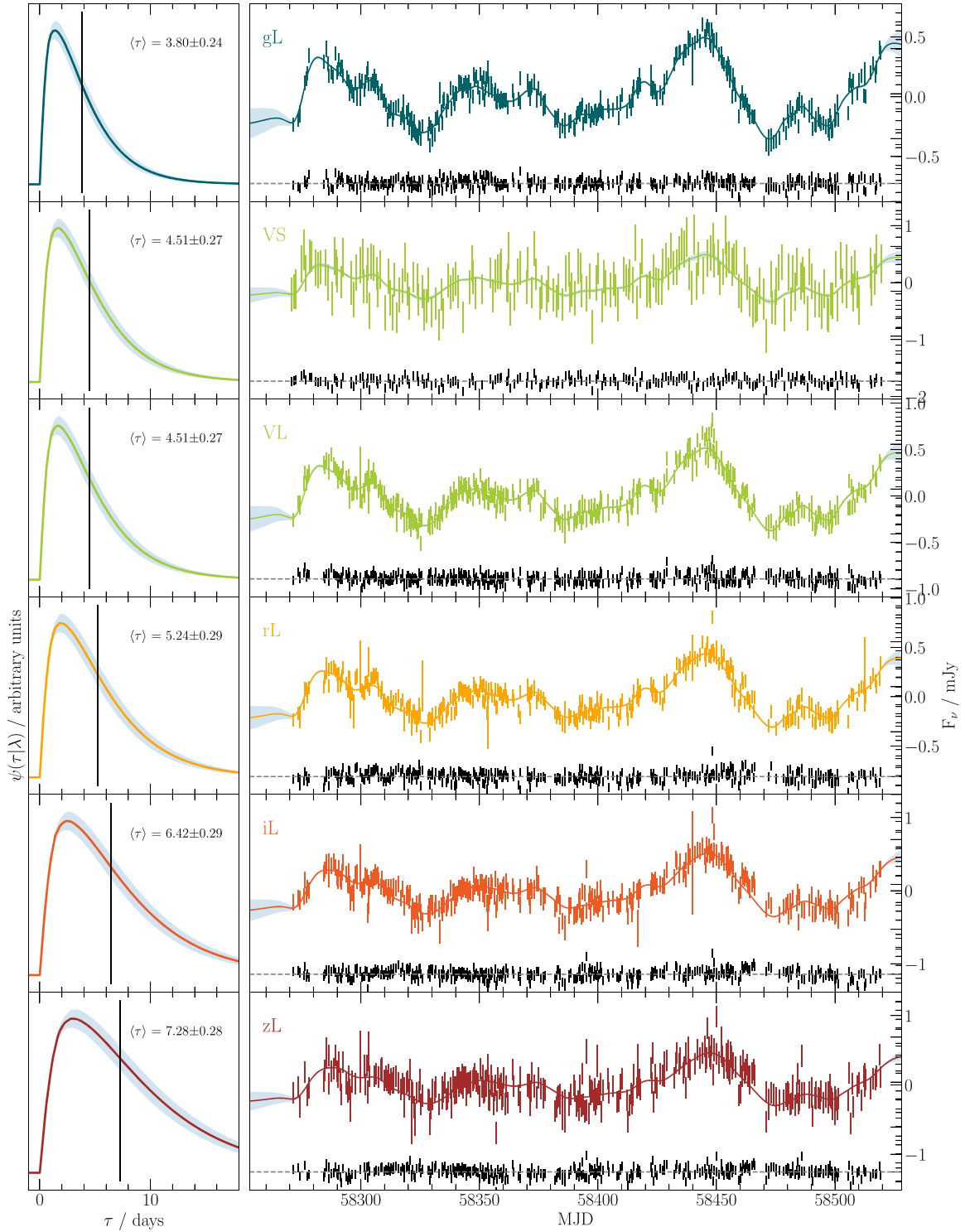
Figure C2. Reverberation model fit with CREAM to a face-on accretion disc and a $T \propto R^{-3/4}$ temperature profile for Fairall 9. The left-hand panels show the delay distribution for each band. The right-hand panel shows the photometry after the quadratic detrend and the best fit. The black points around the dotted grey line show the residuals. All grey envelopes represent the 1σ confidence interval.

APPENDIX D: PARAMETER DISTRIBUTION FOR THE LAG SPECTRUM FIT

We present the joint and marginal posterior distributions of the lag spectrum fit (Fig. D1) described in Section 4.3. We used CORNER.PY (Foreman-Mackey 2016) to visualize the MCMC chains.
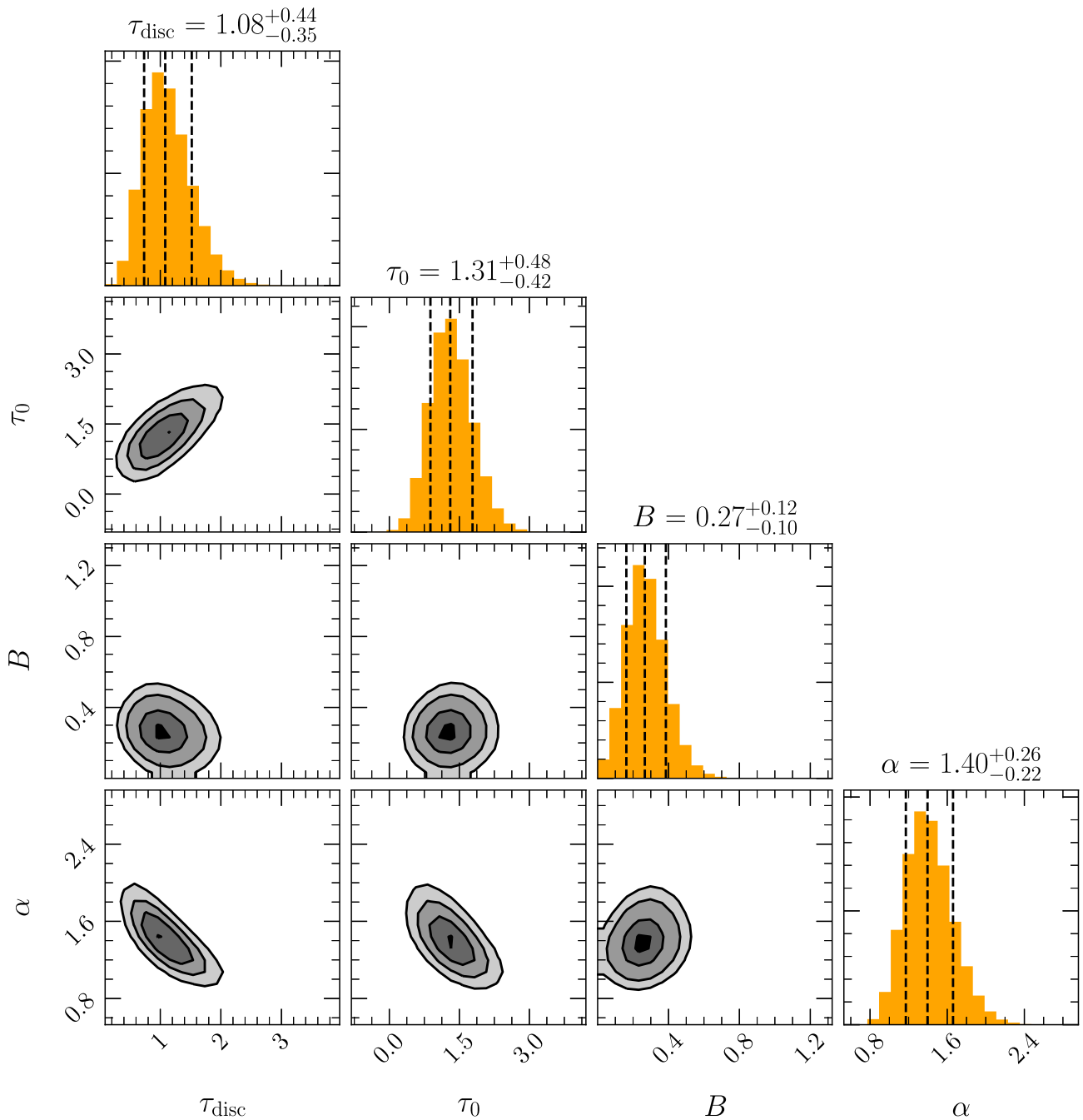
Figure D1. Posterior probability distributions for the accretion disc parameters. Colour scale contours show the joint probability for every combination of parameters. Contours represent the 0.5σ, 1σ, 2σ, and 3σ levels. Marginal posterior distributions are shown as histograms with the median and 1σ marked as dashed lines.

[1] *SUPA Physics and Astronomy, University of St Andrews, Scotland KY16 9SS, UK*

[2] *Department of Astronomy, University of Maryland, College Park, MD 20742-2421, USA*

[3] *Spectral Sciences Inc., 4 Fourth Ave., Burlington, MA 01803, USA*

[4] *Eureka Scientific Inc., 2452 Delmer St, Suite 100, Oakland, CA 94602, USA*

[5] *Department of Physics and Astronomy, 4129 Frederick Reines Hall, University of California, Irvine, CA 92697, USA*

[6] *Department of Physics and Astronomy, Wayne State University, 666 W. Hancock St, Detroit, MI 48201, USA*

[7] *School of Physics and Astronomy, University of Leicester, Leicester, LE1 7RH, UK*

[8] *School of Physics and Astronomy, Raymond and Beverly Sackler Faculty of Exact Sciences, Tel Aviv University, Tel Aviv 69978, Israel*

[9] *Anton Pannekoek Institute, University of Amsterdam, Postbus 94249, NL-1090 GE Amsterdam, the Netherlands*

[10] *Department of Astronomy and Astrophysics, Eberly College of Science, The Pennsylvania State University, 525 Davey Laboratory, University Park, PA 16802, USA*

[11] *Institute of Gravitation and the Cosmos, The Pennsylvania State University, University Park, PA 16802, USA*

[12] *Department of Physics, The Pennsylvania State University, University Park, PA 16802, USA*

[13] *Department of Physics, Western Michigan University, 1120 Everett Tower, Kalamazoo, MI 49008-5252, USA*

[14] *Department of Physics, Montana State University, Bozeman, MT 59717-3840, USA*

[15] *Research School of Astronomy and Astrophysics, Australian National University, Canberra, ACT 2611, Australia*

[16] *Australian Research Council (ARC) Centre of Excellence for All-sky Astrophysics (CAASTRO), Canberra, ACT 2601, Australia*

[17] *Niels Bohr Institute, University of Copenhagen, Juliane Maries Vej 30, DK-2100 Copenhagen Ø, Denmark*

[18] *Dipartimento di Fisica e Astronomia, Università degli Studi di Firenze, Via. G. Sansone 1, I-50019 Sesto Fiorentino (FI), Italy*

[19] *Mullard Space Science Laboratory, University College London, Holmbury St Mary, Dorking, Surrey RH5 6NT, UK*

[20] *Astrophysics Science Division, NASA Goddard Space Flight Center, MC 661, Greenbelt, MD 20771, USA*

[21] *Joint Space-Science Institute, University of Maryland, College Park, MD 20742, USA*

[22] *Dipartimento di Fisica e Astronomia 'G. Galilei', Università di Padova, Vicolo dell'Osservatorio 3, I-35122 Padova, Italy*

[23] *INAF-Osservatorio Astronomico di Padova, Vicolo dell'Osservatorio 5, I-35122 Padova, Italy*

[24] *Department of Physics, University of Kentucky, Lexington, KY 40506, USA*

[25] *Instituto de Astronomía, Universidad Nacional Autónoma de México, Km 103 Carretera Tijuana-Ensenada, 22860 Ensenada B.C., México*

[26] *Department of Earth and Space Sciences, Morehead State University, 235 Martindale Drive, Morehead, KY 40351, USA*

[27] *Department of Physics and Astronomy, N283 ESC, Brigham Young University, Provo, UT 84602-4360, USA*

[28] *Space Telescope Science Institute, 3700 San Martin Dr., Baltimore, MD 21218, USA*

[29] *Department of Astronomy and Astrophysics, The Pennsylvania State University, University Park, PA 16802, USA*

[30] *Department of Astronomy, The Ohio State University, 140 W 18th Ave., Columbus, OH 43210, USA*

[31] *Center for Cosmology and AstroParticle Physics, The Ohio State University, 192 West Woodruff Avenue, Columbus, OH 43210, USA*

[32] *Astrophysics Science Division, NASA Goddard Space Flight Center, Greenbelt, MD 20771, USA*

[33] *SRON Netherlands Institute for Space Research, Sorbonnelaan 2, NL-3584 CA Utrecht, the Netherlands*

[34] *Department of Physics, University of California, Davis, CA 95616, USA*

This paper has been typeset from a TEX/LATEX file prepared by the author.